Atomistic spin dynamics simulations of magnonic spin Seebeck and spin Nernst effects in altermagnets

Markus Weißenhofer [1,2,*] and Alberto Marmodoro [3]

[1]*Department of Physics and Astronomy, Uppsala University, P. O. Box 516, S-751 20 Uppsala, Sweden*

[2]*Department of Physics, Freie Universität Berlin, Arnimallee 14, D-14195 Berlin, Germany*

[3]*Institute of Physics, Czech Academy of Sciences, Cukrovarnická 10, 162 00 Praha 6, Czech Republic*

(Received 11 June 2024; revised 28 August 2024; accepted 5 September 2024; published 19 September 2024)

Magnon band structures in altermagnets are characterized by an energy splitting of modes with opposite chirality, even in the absence of applied external fields and relativistic effects, because of an anisotropy in the Heisenberg exchange interactions. We perform quantitative atomistic spin dynamics simulations based on *ab initio* electronic structure calculations on rutile RuO_2, a prototypical "d-wave" altermagnet, to study magnon currents generated by thermal gradients. We report substantial spin Seebeck and spin Nernst effects, i.e., longitudinal or transverse spin currents, depending on the propagation direction of the magnons with respect to the crystal, together with a finite spin accumulation associated with nonlinearities in the temperature profile. Our findings are consistent with the altermagnetic spin-group symmetry, as well as predictions from linear spin-wave theory and semiclassical Boltzmann transport theory.

DOI: 10.1103/PhysRevB.110.094427

I. INTRODUCTION

The study of magnons, low-energy collective excitations of magnetic systems, offers important insight into fundamental properties of condensed matter systems. In addition to that magnons have been extensively explored in light of their potential for novel applications [1–6]. These efforts lead to the foundation of the field of *magnon spintronics*, which aims at developing energy-efficient information storage and processing strategies by eliminating energy loss caused by Joule heating associated with charge transport.

Magnons in ferromagnetic materials are characterized by a well-defined chirality, as a result of time-reversal symmetry breaking, and can hence carry spin currents, enabling their usage for magnon spintronics [1]. However, their dispersion relation is typically quadratic, rendering the group velocity wave vector dependent and thus hindering the propagation of stable magnon wave packets.

Antiferromagnetic magnons, on the other hand, typically have a linear dispersion relation close to the center of the Brillouin zone, as long as relativistic effects are neglected, and reach the THz regime [7,8]. Because of conserved symmetry under inversion and time reversal, the corresponding two magnon modes with left- and right-handed chirality are degenerate across the entire Brillouin zone in conventional collinear antiferromagnets [9]. Hence, the observation of magnon currents carrying finite spin angular momentum requires either an externally applied magnetic field [10–12], or the presence of higher-order exchange interactions, such as, e.g., the Dzialoshinskii-Moriya interaction. The latter introduces a directional modulation (or nonreciprocity) of the dispersion relation [13,14]. The magnitude of this modulation will, however, depend, approximately, on the strength of spin-orbit coupling (SOC).

We turn therefore our attention to altermagnetism, which has been recently established as a special case of collinear antiferromagnetism that is characterized by a spin-split band structure for electrons [15,16] and magnons [17,18], even in the absence of relativistic effects and external fields. In the presence of crystal-field splitting acting along different directions on antiparallel magnetic atoms, the (scalar) Heisenberg exchange interactions can also pick up a sizable direction dependence, i.e., anisotropy, even regardless of SOC [19]. As a consequence, one can predict that the magnon dispersion will be, in general, nondegenerate across the Brillouin zone, except for a marginal set of $\boldsymbol{k}$ points [15,20] (corresponding to, e.g., nodal planes, and depending on the specific spin-group symmetry of the ground state), as schematically illustrated in Fig. 1.

As for any collinear antiferromagnet, the wave-like precession of atomic magnetic moments will involve to variable extent, in general, the different magnetic sublattices as a function of $\boldsymbol{k}$: Approaching the boundary of the Brillouin zone, magnons will tend to be hosted exclusively by one or by the other sublattice, while they will equally involve both of them towards the Γ point. Away from it, the different, now energy-split two magnon dispersions describe excitations that carry (spin) angular momentum with opposite sign [17,21–23]. This can pave the way for a variety of concept applications revisiting earlier proposals, initially put forward, based on the different, higher-order Heisenberg exchange interactions route in order to achieve nonreciprocity [24].

*Contact author: markus.weissenhofer@fu-berlin.de

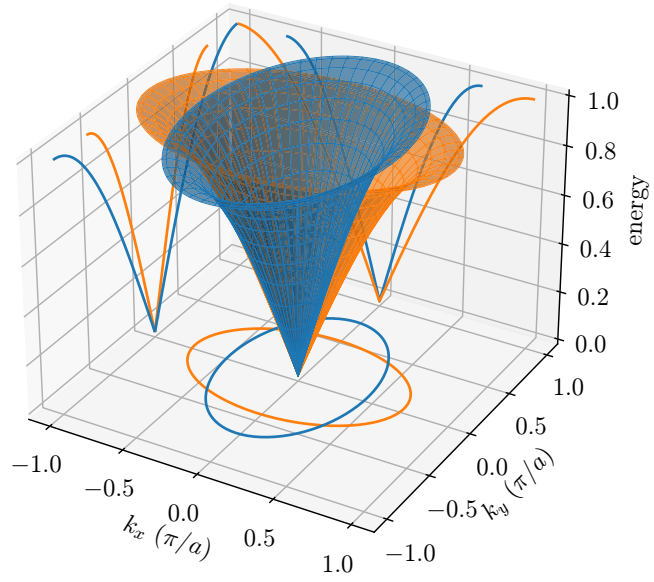

FIG. 1. Schematic representation of the magnon dispersion in "d-wave" altermagnets, such as in particular in the case of rutile unit cells. The dispersion of both magnon modes is linear around the Γ point, with an alternating frequency split across the Brillouin zone. The solid lines correspond to sections through the dispersion relation for some constant energy (projected onto the k_x, k_y plane), for $k_y = 0$ (k_x, energy plane) and for $k_x = 0$ (k_y, energy plane).

Of course, in a real sample both SOC-driven and crystal-field-driven mechanisms for anisotropic exchange interactions would normally occur concurrently.

In this paper, we aim to investigate magnon currents in altermagnets by means of quantitative *ab initio* electronic structure and atomistic spin dynamics calculations, as well as by analytical linear spin-wave theory derivations. We will study the steady spin current set in motion by a thermal gradient between two heat reservoirs mediated by magnons, i.e., the magnon spin Seebeck and spin Nernst effects [18].

In particular, we will examine how these emerge as a function of relative direction between temperature gradient, anisotropy in the (scalar) Heisenberg exchange interactions, and the resulting nondegenerate magnon dispersion. This scenario is realized by altermagnets in full analogy with their energy split and alternating spin-polarized electronic band structure and beside possible further effects proportional to SOC [25,26], because of the interplay between orientation of crystal field splitting from nonmagnetic atoms, which introduces strong anisotropy in the magnetization density [15,27,28], and the direction of antiparallel magnetic sublattices.

We adopt as prototype material for our calculations the example of rutile RuO_2. While other studies have started to examine electronic-mediated thermal transport [29], we focus here on the magnonic degree of freedom of altermagnets. In addition to its thermally generated, magnon-mediated steady-state spin currents between two heat reservoirs, our simulations also predict the emergence of a finite local magnetic moment, or spin accumulation, in correspondence with nonlinearities in the temperature gradient profile.

This paper is structured as follows. We begin by recalling the essential features of this material, highlighting those aspects that qualify it as an altermagnet. In particular, details for the spin model parameters and the ensuing magnon dispersion for RuO_2 are given in Sec. II. Theoretical methods used for the simulation of magnon dynamics because of temperature gradients in terms of a stochastic Landau-Lifshitz-Gilbert equation of motion are briefly introduced in Appendix C. We then report numerical results from such atomistic spin dynamics simulations (Sec. III). These are also confirmed through comparison with predictions from linear spin-wave theory, in combination with semiclassical Boltzmann transport theory (Appendix B). We then summarize our findings and offer our conclusions (Sec. IV).

II. MAGNON DISPERSION IN RuO_2

We perform numerical calculations based on *ab initio* electronic structure calculations and atomistic spin dynamics, in order to provide a realistic estimate of magnon-mediated Seebeck and Nernst effect associated with the nonrelativistic component of nondegenerate spin-wave dispersion in altermagnets [17,22].

We choose in particular RuO_2 as prototype altermagnet [30], because of the growing body of theoretical and experimental literature dedicated to this compound. This material received initial attention because of its metallic conductivity, relatively rare for oxides, in combination with reports of collinear antiferromagnetic order up to room temperature [31], leading to high expectations for possible electron-mediated spintronics applications [29,32–35].

On the other hand, this paper focuses on transport properties mediated by magnons, not by electronic charge carriers. Other spin-split antiferromagnets (or altermagnets) with a gap at the Fermi level, but with alike unit-cell geometry and magnetic order (such as, e.g., MnF_2, FeF_2, or CoF_2, just to remain within the subclass of rutile structures), would also be valid candidate materials. Our conclusions will also apply, qualitatively, to cases with more than two sublattices with antiparallel magnetic moments and/or with a symmetry different from fourfold rotation, such as in the examples of ferric oxide Fe_3O_4, or of MnTe [17].

RuO_2 crystallizes in the rutile structure, see Fig. 2(a), with two opposite-spin sublattices [31], as further discussed in Refs. [36–38]. Because of the nonmagnetic atoms occupying the Wyckoff position $4f$, equivalence between Ru_1 and Ru_2 cannot be achieved through pure time reversal, i.e., flipping the sign of the Néel vector, but only when this symmetry operation is also accompanied by a space rotation, by 90° in this rutile example geometry. The requirement of such combination of time and space symmetry operations characterizes altermagnets, in comparison with conventional collinear antiferromagnets.

In this paper we adopt RuO_2 Heisenberg exchange parameters calculated from density functional theory in its spin-polarized relativistic Korringa-Kohn-Rostoker implementation by means of the magnetic force theorem, in the same fashion as Ref. [17]. For details, see Appendix E.

In the corresponding Heisenberg Hamiltonian

$$\mathcal{H} = -\sum_{ij}\sum_{ss'} J_{ij}^{ss'} \boldsymbol{S}_{is} \cdot \boldsymbol{S}_{js'}, \tag{1}$$

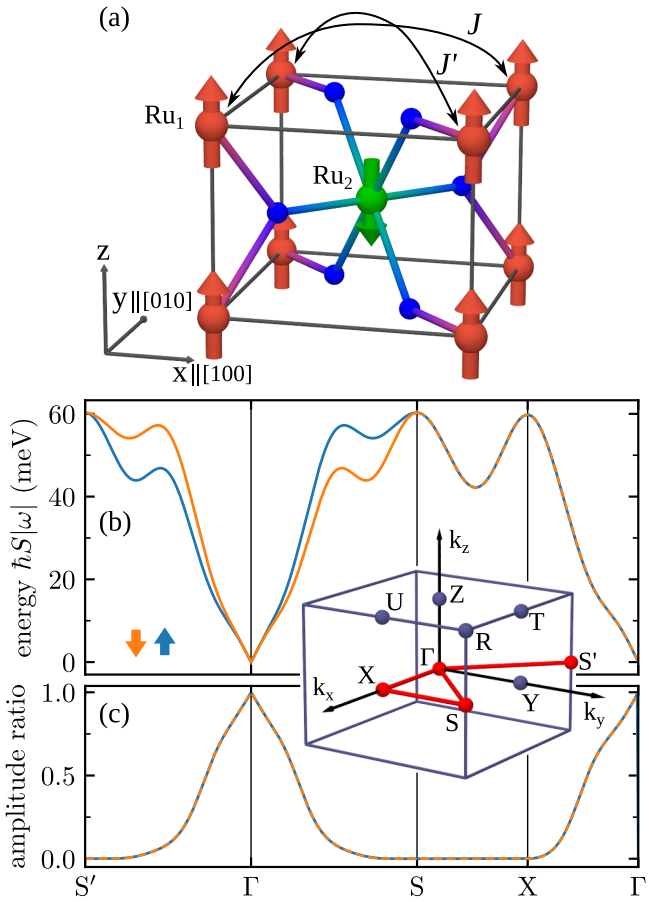

FIG. 2. (a) Unit cell of the altermagnetic rutile phase of RuO_2. Collinear antiparallel magnetic order across Ru sublattices is represented via red and green colors and arrows. Nonmagnetic O atoms are depicted as smaller blue spheres. The most significant anisotropic Heisenberg exchange interactions J, J' are also highlighted via thin-black arrows. (b) Magnonic band structure of RuO_2 shown along a Brillouin-zone path (inset, highlighted in red) within the k_x–k_y plane crossing the Γ point. The bold arrows indicate the net spin of the modes. (c) Corresponding amplitude ratio between the tilting of the Ru moments at each sublattice.

$J_{ij}^{ss'}$ denotes scalar coupling constants, and $\boldsymbol{S}_{is}$ is a unit vector describing the direction of the Ru magnetic moment at position $\boldsymbol{r}_i + \boldsymbol{b}_s$, with $\boldsymbol{r}_i$ being the location of the unit cell within the periodic lattice, and $\boldsymbol{b}_s$ the sublattice position within the unit cell. The full list of Heisenberg exchange parameters can be found in Appendix E.

Notably, exchange constants between atomic magnetic moments at relative position $\boldsymbol{R}_{ij}^{ss'} = \boldsymbol{r}_j - \boldsymbol{r}_i + \boldsymbol{b}_{s'} - \boldsymbol{b}_s$ not only depend on their distance $|\boldsymbol{R}_{ij}^{ss'}|$, but also on the direction of $\boldsymbol{R}_{ij}^{ss'}$. In this particular example, this is mainly because of the occurrence of O atoms in the low-symmetry Wyckoff $4f$ position. Their biggest influence can be noted for the intra-sublattice exchange constants between Ru atoms at a distance of $|\boldsymbol{R}_{ij}^{ss'}| = \sqrt{2}A_{\text{lat}}$ (with A_{lat} being the length of the edge for the square unit-cell section in the x, y plane of a rutile lattice). This displacement vector either intersects oxygen atoms along the [110] direction, or it passes in-between them along the orthogonal $[\bar{1}10]$ direction, or vice versa for the other sublattice [Fig. 2(a)].

We calculate here the magnon band structure from the spin Hamiltonian Eq. (1), using the Holstein-Primakoff transformation up to second order in magnon variables and diagonalizing the resulting Hamiltonian via the Bogoliubov-Valatin transformation [9]. The eigenenergies of both magnon branches along different paths of the k_x, k_y Brillouin-zone section are shown in Fig. 2(b) for $k_z = 0$. Similar to the results of Ref. [17], we obtain a linear dispersion close to the Γ point, and a characteristic energy splitting of the magnon branches away from nodal manifolds of the Brillouin zone, which for this rutile geometry coincide for instance with the k_x, k_z or with the k_y, k_z planes. The corresponding eigenfrequencies have opposite sign along each of the two branches, i.e., the Ru moments of the first sublattice rotate in opposite direction with respect to the moments of the second sublattice (Fig. 3).

This angular velocity defines the chirality of each branch, and it corresponds to the angular momentum carried by each magnon mode. We denote here as right handed the counterclockwise rotation of the Ru moment on the first sublattice, and conversely we denote as left handed the opposite, clockwise rotation.

These two possible chiralities are accompanied by a different tilting away from the ground-state direction for the Ru moments at each sublattice. Upon approaching the Brillouin-zone boundary, the magnon modes involve tilting and precession for the atomic magnetic moments of only one or only the other Ru sublattice. Conversely, in the limit $\boldsymbol{k} \to \Gamma$ both sublattices are equally affected, eventually realizing a twofold degenerate Goldstone mode, which costs zero-energy when neglecting magnetocrystalline anisotropy (MCA), and in which the Néel vector precesses while remaining straight (Fig. 3).

Away from these two extremes, i.e., for generic $\boldsymbol{k}$ points, the magnitude of tilt away from ground-state magnetization direction for the two antiparallel Ru sublattices, i.e., their involvement in hosting the magnon excitation, varies continuously. In the following, we quantify it as the ratio between the smaller and the larger tilt, which lies within the interval [0,1]. In other words, for one magnon chirality it is the ratio between the deviation from the ground-state magnetization direction of Ru_1 atoms, compared to the deviation of Ru_2 atoms; and vice versa for the other magnon chirality.

We note that, although the amplitude ratio varies throughout the Brillouin zone [Fig. 2(c)], the net angular momentum carried by each magnon is either $+1$ or -1 along the z direction, depending only on the chirality of the magnon branch and not on $\boldsymbol{k}$. Additional information on the calculation of the magnon band structure can be found in Appendix A.

III. SIMULATION RESULTS

In order to account for a thermal gradient, in the following we resort to atomistic spin dynamics simulations based on the time-evolution of the stochastic Landau-Lifshitz-Gilbert (sLLG) equation of motion [39–41]. This describes the dynamics of the Ru magnetic moments coupled to a heat bath (see Appendix C, for details). In particular, a thermal gradient is simulated by assuming that each moment, within a large ensemble of replicas for the RuO_2 unit cell, is coupled to

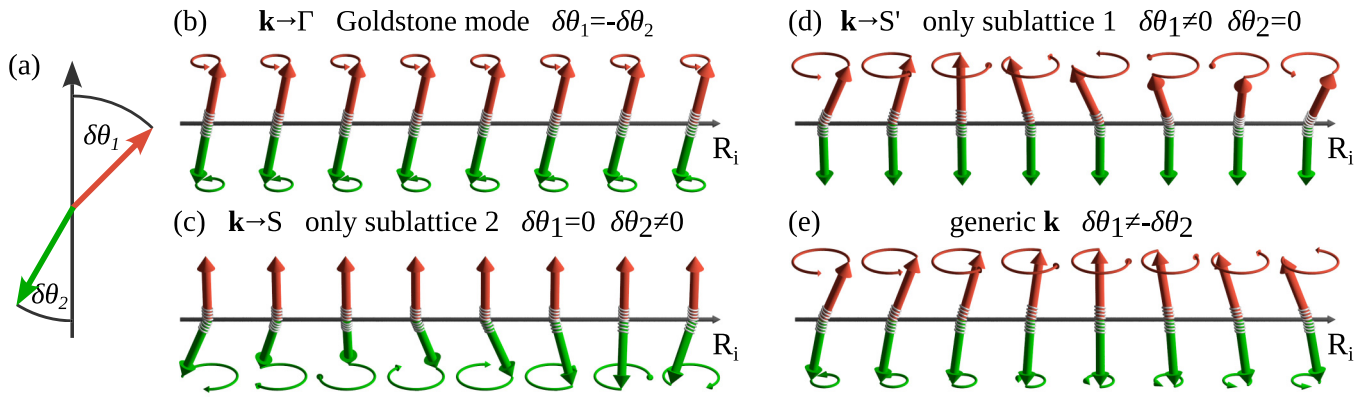

FIG. 3. Schematic depiction of the precessing atomic magnetic moments from antiparallel Ru sublattices (red or green arrows), belonging to a magnon eigenmode with wave vector $\boldsymbol{k}$. (a) Their deviation from the ground-state magnetic order is given by the azimuth angle $\delta\theta$ via $S_n^z = \cos(\theta_n + \delta\theta_n)$, where $\theta_1 = 0$ and $\theta_2 = \pi$ for the two magnetic sublattices. (b) In the $\boldsymbol{k} \to \Gamma$ limit, both tilts are the same. [(c), (d)] Upon approaching the Brillouin-zone boundary, the excitations involve predominantly only one or only the other sublattice, with largest difference along $\Gamma \to S$ or vice versa along the orthogonal $\Gamma \to S'$ directions. (e) For generic $\boldsymbol{k}$, both tilt angles are finite but different.

its own heat bath with a fixed temperature, which varies as a function of position [42–49].

As further discussed below, magnons will in general flow from the hot to the cold terminals, maintaining a steady current regime across the two heat reservoirs.

In this case study we examine this effect as a function of both changing the steepness of the thermal gradient, and its direction relative to the crystal lattice. As a first temperature profile we consider the limiting case of a very abrupt temperature step, with a sudden drop in temperature between hot and cold region. We then repeat simulations for the more realistic case of a gradual, linear temperature slope spanning many unit cells.

We consider the direction of these temperature profiles both along the [100] and along the [110] axis of the lattice, which correspond, respectively, to energy-degenerate or to energy-split magnon dispersions in reciprocal space (see Fig. 2).

In all these cases we examine in particular the time average of net magnetization per RuO_2 unit cell at a given temperature, i.e., within the same layer perpendicular to the direction of the chosen thermal profile. In general, this will be nonzero when the tilt of either Ru atoms away from ±z ground-state direction is inequivalent. We then also estimate the similarly layer-resolved longitudinal spin current, which can again be nonzero because of the flow from hot to cold regions of more magnons with a given chirality than with the opposite one.

We begin with results for the thermal profile characterized by an abrupt temperature step (Fig. 4). When this thermal profile is aligned along the direction corresponding to the maximal energy splitting between the two magnon eigenmodes, i.e., along the [110] direction (or conversely, along [$\bar{1}$10]), we observe the largest unbalance in the flow of magnons propagating in the same hot-to-cold direction, but with opposite chirality. As a result, we obtain a numerical demonstration of a magnon-mediated spin Seebeck effect [45,50], now associated with anisotropic scalar Heisenberg interactions and altermagnetic low symmetry of bulk RuO_2, rather than higher-order exchange terms such as, e.g., DMI, which scale in magnitude with the strength of SOC.

We observe peaks in the spin accumulation, i.e., the net magnetization per unit cell, in the vicinity of the temperature step [Fig. 4(b)]. These peaks get reproduced with opposite sign upon rotating the thermal profile from [110] to [$\bar{1}$10] direction.

On the other hand, if the direction of the temperature profile is aligned with any nodal plane for the magnon band structure, such as, e.g., with the [100] direction, we still have a magnon current from hot to cold regions, but no transport of angular momentum. This is a consequence of populating the Bose-Einstein statistics with equal number of magnons with opposite chirality, leading to zero net angular momentum current and zero emerging net magnetization per unit cell along the whole thermal profile.

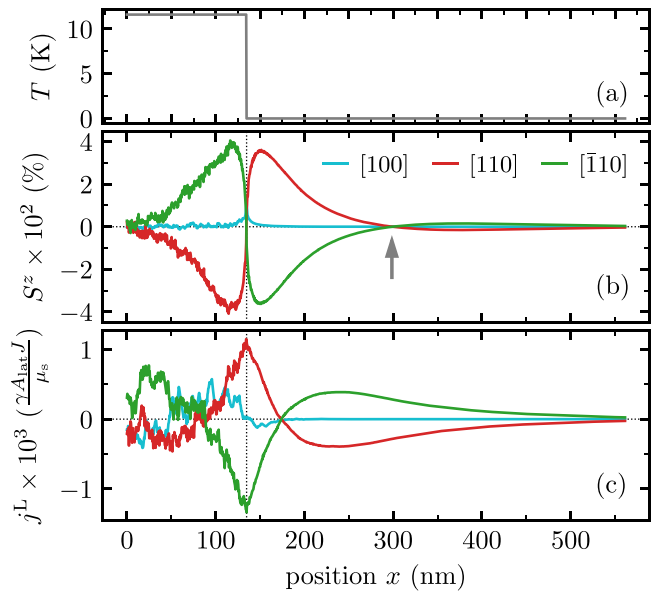

FIG. 4. Simulated abrupt temperature profile (a), local magnetic moment as a percentage of the ground-state magnetic moment (b), and longitudinal spin current (c), for different crystallographic directions (color coded). The grey arrow marks the sign switch of the emergent magnetization.

The above features, within numerical accuracy and statistics of the sLLG treatment, are in accordance with the time reversal and fourfold space rotation symmetries of altermagnetic RuO_2.

Returning to the case of the abrupt thermal profile (Fig. 4) we also observe a sign change in the emergent magnetization at a certain distance $\Delta = x - x_0$ from the temperature step at x_0. This feature occurs at the same distance when simulations are performed along orthogonal directions, e.g., along [110] and [$\bar{1}$10], which both correspond to thermal gradient orientations leading to the largest Seebeck effect.

We interpret it as evidence of competition between the two magnon bands, which coexist but contribute to a different extent and with opposite sign to the net spin current. In terms of Boltzmann transport theory we have

$$S^z(x) = \sum_{\boldsymbol{k}} n_{\boldsymbol{k}}^{\beta}(x) - n_{\boldsymbol{k}}^{\alpha}(x), \tag{2}$$

where α and β denote the left- and right-handed magnon chirality, and $n_{\boldsymbol{k}}^{\alpha(\beta)}(x)$ is the position-dependent number of magnons.

In this first case of an abrupt thermal gradient, we obtain $n_{\boldsymbol{k}}^{\alpha(\beta)}(x) = n_{\boldsymbol{k}}^{\alpha(\beta)}(x_0)e^{-(x-x_0)/\lambda_{\boldsymbol{k}}^{\alpha(\beta)}}$, i.e., an exponential decay in the number of magnons as a function of distance from the abrupt temperature drop at x_0, with chirality-dependent decay length $\lambda_{\boldsymbol{k}}^{\alpha(\beta)}$.

As shown in Appendix B, this formula qualitatively reproduces the features of the emergent magnetization depicted in Fig. 4(b) from numerical solution of the stochastic LLG equation of motion. In particular, the key parameters controlling the sign and magnitude of the emergent magnetization are the occupation number (which itself depends on the temperature at each x), the decay length and the chirality-dependent spin angular momentum from the magnon band structure.

Within the same framework of Boltzmann transport theory, an expression for the spin current,

$$\boldsymbol{j}(x) = \sum_{\boldsymbol{k}} n_{\boldsymbol{k}}^{\beta}(x)\boldsymbol{v}_{\boldsymbol{k}}^{\beta} - n_{\boldsymbol{k}}^{\alpha}(x)\boldsymbol{v}_{\boldsymbol{k}}^{\alpha}, \tag{3}$$

in terms of number of magnons and their group velocity $\boldsymbol{v}_{\boldsymbol{k}}^{\alpha(\beta)} = \partial\omega_{\boldsymbol{k}}^{\alpha(\beta)}/\partial\boldsymbol{k}$ for each chirality can also be introduced. This quantity is not explicitly computed within atomistic spin dynamics calculations, which only provide the values of an ensemble of atomic moments $\boldsymbol{S}_{is}(t)$ over the chosen interval of time.

Following the template of Refs. [1,51] for ferromagnets, we therefore introduce the following quantity:

$$j^{\mu}(\boldsymbol{r}_i) = -\frac{\gamma}{\mu_s}A_{\text{lat}}J(\langle \boldsymbol{S}_{i\text{a}} \times \boldsymbol{S}_{i+1,\text{a}}\rangle + \langle \boldsymbol{S}_{i\text{b}} \times \boldsymbol{S}_{i+1,\text{b}}\rangle) \cdot \boldsymbol{e}_{\mu}, \tag{4}$$

where the average $\langle \ldots \rangle$ is performed over time and $J := J_{i,i+1}^{\text{aa}} = J_{i,i+1}^{\text{bb}}$, with a, b being sublattice indices. The parameters μ_s and γ are the saturation magnetic moment and the gyromagnetic ratio. Eq. (4) describes the transfer of the μth component of the spin angular momentum from the unit cell i (located at $\boldsymbol{r}_i$) to the adjacent unit cell $j = i + 1$ and can thus be used to estimate the spin current along different spatial directions $\boldsymbol{r}_{ij} = \boldsymbol{r}_j - \boldsymbol{r}_i$. Note that we have neglected here the intersublattice correlations $\langle \boldsymbol{S}_{is} \times \boldsymbol{S}_{i+1,s'\neq s}\rangle$, which we found to be much smaller than the intrasublattice correlations. A detailed discussion as well as the derivation of Eq. (4) can be found in Appendix D.

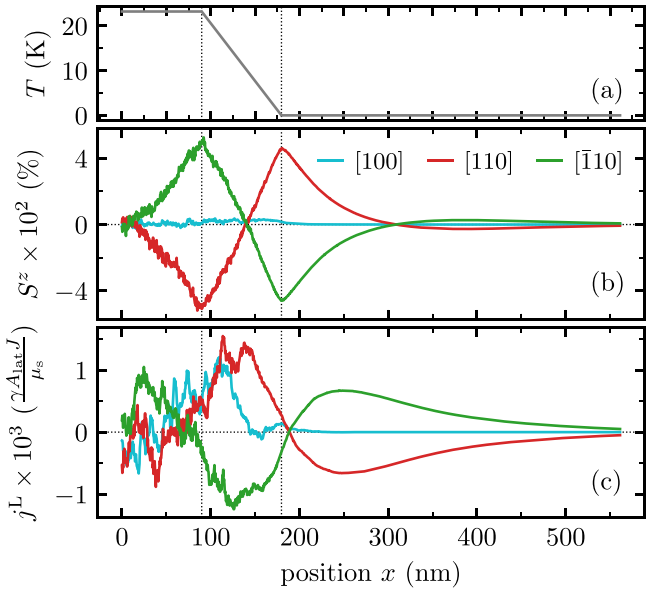

FIG. 5. Simulated linear temperature gradient profile (a), local magnetic moment (b), and longitudinal spin current (c), again for different crystallographic directions (color coded).

Results from this equation for the spin current, selecting in particular the z spin component of the longitudinal current j^{L}, are shown in Fig. 4(c) for the abrupt thermal drop profile along different crystallographic directions. In the product between statistically sampled moments at positions $\boldsymbol{r}_i$ and $\boldsymbol{r}_{i+1}$, the effect of stochastic fluctuations gets magnified leading to a more noisy outcome, more pronounced in the high-temperature regime. We also expect that j^{L} should average to zero over the whole x range when the thermal profile is aligned along the [100] direction; but this appears to require an increase in the system size and/or the sLLG simulation time beyond the scope of this paper.

For the [110] and [$\bar{1}$10] orientations of the thermal profile, the spin current has an extremum directly at the step. Its sign follows from the sign of emergent magnetization in Fig. 4(b), because of the propagation of the current always from hot to cold [18]. Same as S^z, the longitudinal spin current shows a flip in sign, but closer to the thermal drop at x_0. We obtain three extrema of j^{L}, same as the number of zero crossing of S^z. This feature is consistent with Boltzmann transport theory within the constant relaxation time approximation, which for a steady-state solution prescribes $-\partial_x j^{\text{L}} \propto S^z$ (see Appendix B).

We then repeat calculations for a more realistic setup where the two heat reservoirs are connected by a thermal gradient with linear slope over a finite thickness [Fig. 5(a)]. The emergent z magnetization reproduces some of the features of the previous scenario of an abrupt drop in temperature (Fig. 4), such as the relationship between the sign of S^z and the direction of the thermal profile.

The main difference is that S^z changes linearly within the region with the linear temperature gradient, with peaks

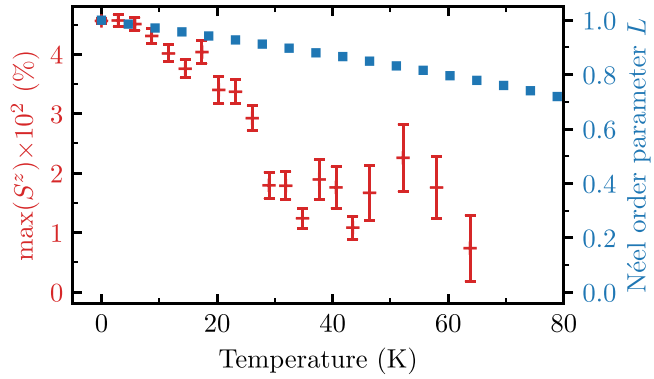

FIG. 6. Maximum of spin accumulation for a linear temperature gradient in [110] orientation (red) and Néel order parameter (blue) vs temperature.

exactly at the kinks of the temperature profile [Fig. 5(b)]. Qualitatively, the position and sign of these peaks can be understood using again linear spin-wave theory and Boltzmann transport theory. Within this framework, the spin current is proportional to the temperature gradient $j^{\mathrm{L}} = \sigma^{\mathrm{L}}\partial_x T$, with σ^{L} being the longitudinal component of the magnon spin conductivity [18], and, same as above, $-\partial_x j^{\mathrm{L}} \propto S^z$. Combining the two expressions, we obtain $S^z \propto -\sigma^{\mathrm{L}}\partial_x^2 T$. This means that the emergence of a finite S^z requires nonlinearities of the temperature profile.

However, while this simple formula is helpful in predicting whether a finite magnetization emerges at all, it cannot explain its length scales. Quantitative values require numerical sLLG simulations.

We also want to point out that a longitudinal spin current could, in principle, lead to a spin accumulation at the edge of the system in propagation direction. Since in the scenario considered here the magnon propagation length is shorter than the region of constant temperature at the cold end of the system, the magnon current is effectively damped before possibly accumulating at the edges.

Next, we want to discuss the temperature scaling of the spin Seebeck effect by adding a constant temperature offset to the linear temperature gradient profile depicted in Fig. 5(a) in the [110] orientation. We quantify the strength of the spin Seebeck effect via the maximum of the spin accumulation at the right kink of the temperature profile, which we obtain by fitting $S^z(x > x_0) = A_\beta e^{-(x-x_0)/\lambda^\beta} - A_\alpha e^{-(x-x_0)/\lambda^\alpha}$ to the spin accumulation in the constant temperature regime to the right of the linear gradient. This expression is inspired by the two-current picture of the Boltzmann transport theory [cf. Eq. (2)] and is found to agree remarkably well with the simulation data. The maximum of the spin accumulation is calculated as $A_\beta - A_\alpha$ and shown in Fig. 6 versus temperature offset. In contrast to what was reported in Ref. [18], where a substantial increase of the spin Seebeck coefficient with temperature was reported, spin accumulation is significantly reduced with increasing temperature. We attribute this discrepancy to the fact that the authors of Ref. [18] used linear spin-wave theory, where temperature only affects the magnon population via the Bose-Einstein distribution, whereas here we use the nonlinear stochastic LLG, which automatically includes all

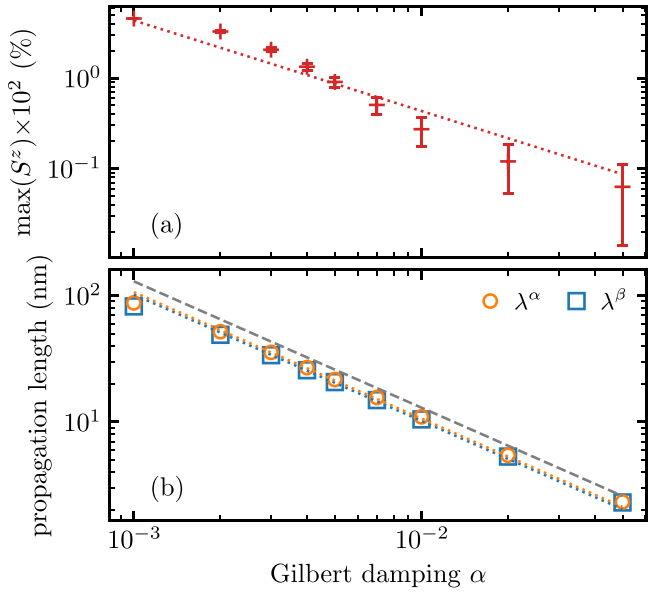

FIG. 7. Maximum of spin accumulation (a) and propagation lengths $\lambda^{\alpha(\beta)}$ (b) vs Gilbert damping parameter α for a linear temperature gradient in [110] orientation. Dotted lines are fits of $\propto \alpha^{-1}$ to the data and serve as guide to the eye and the grey dashed line is the relation $\lambda = A_{\mathrm{lat}}/(2\sqrt{3}\alpha)$.

higher-order magnon terms responsible for magnon-magnon scattering and magnon softening. Comparison with the temperature scaling of the Néel order parameter (see Appendix C for details) reveals that the drop of the spin Seebeck effect with temperature cannot be fully explained by a thermally induced renormalization of the effective spin length, but that other effects—most likely a reduction of the magnon lifetime because of magnon-magnon scattering—also play a role. This is further underlined by the fact that the propagation lengths $\lambda^{\alpha(\beta)}$ obtained by the fitting procedure described above drop by more than 15% above 20 K.

The impact of Gilbert damping on the spin Seebeck effect is addressed in Fig. 7. Again, we consider a linear temperature gradient profile as shown in Fig. 5(a) in the [110] orientation. As can be seen in Fig. 7(a) from the maximum of the spin accumulation (obtained from the same fitting procedure as above), the magnitude of the spin Seebeck effect is strongly reduced by a higher Gilbert damping, because of the impact of Gilbert damping on the magnon lifetimes and the propagation lengths [see Fig. 7(b)]. The latter roughly obey the relation $\lambda = A_{\mathrm{lat}}/(2\sqrt{3}\alpha)$, which was derived as an approximation of the magnon propagation length in conventional antiferromagnets in Ref. [51]. Note that, irrespective of Gilbert damping, we find that $\lambda^\alpha > \lambda^\beta$, giving rise to the sign change of the spin accumulation at an α-dependent distance from the temperature gradient, visible in Figs. 4(b) and 5(b).

We finally investigate the generation of transverse spin currents j^{T} via the spin Nernst effect. In a recent study [18] it has been predicted that strength of the spin Nernst effect in altermagnets can be significantly larger than in other collinear antiferromagnets, where it emerges because of nonzero Berry curvature [52,53].

In Fig. 8 we depict results for the transverse spin current obtained using Eq. (4) for the same temperature step profile

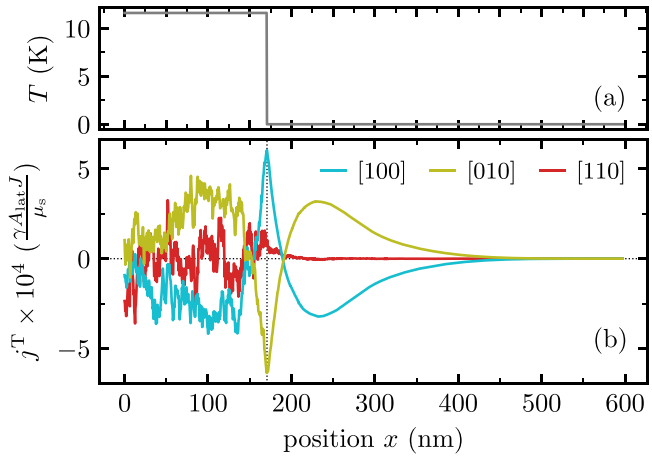

FIG. 8. Simulated abrupt temperature profile (a) and transversal spin current (b), for different crystallographic directions (color coded).

discussed above. In line with the predictions of [18], our simulations clearly show that only magnon currents traveling along the [100] and [010] directions lead to the emergence of a transverse spin current. The fluctuating values of j^{T} for the [110] case can be attributed to the aforementioned slow convergence of this quantity. This is underlined by calculations within Boltzmann transport theory (shown in Appendix B), which support our numerical findings for the [100] and [010] cases and predict a vanishing transverse spin current for the [110] case. Remarkably, the spatial profile of the transverse spin current is found to be very similar to the one of the longitudinal spin current, with a magnitude that is roughly a factor two smaller.

Note that in our simulations the emerging transverse spin current cannot lead to a finite spin accumulation, because of the lack of translational symmetry breaking along the transverse direction. This is because we use periodic boundary conditions along y, z, i.e., perpendicularly to the direction x of the temperature profile, in order to reduce possible numerical artifacts because of finite simulation size. The simulation of real 2D (or even 3D) systems with diameters of several hundred nanometres (containing more than 10^8 Ru moments) is beyond the scope of this work. Real systems, of course, are finite and thus we expect that the transverse spin current results in a spin accumulation—a finite net magnetization—with the same spatial profile (with opposite sign) at the opposing edges. We propose that this spin accumulation could be experimentally detected using, e.g., magneto-optical measurement analogous to the detection of spin [54] or orbital Hall effects [55,56].

IV. CONCLUSIONS

We predict that spin-split antiferromagnets (or altermagnets) host magnon currents traveling from the hot to the cold reservoirs. Specific to this class of materials, the nondegenerate, chirality-dependent energy splitting of the magnon band structure, which is present even in the absence of higher order Heisenberg Hamiltonian terms (such as, e.g., Dzialoshinskii-Moriya interactions), leads to different propagation of magnons with antiparallel spin angular momentum depending on the direction of the thermal gradient with respect to the crystal, and in particular to the anisotropy in the nonrelativistic (scalar) Heisenberg exchange interactions.

This outcome is consistent with the symmetry of the spin currents and the ensuing spin accumulation according to spin-group analysis, and it has been both quantitatively explored through numerical stochastic Landau-Lifshitz-Gilbert (sLLG) calculations based on parameters from ab initio electronic structure theory, and through Boltzmann transport theory in the constant relaxation time approximation.

In particular, we provide an estimate of magnon-mediated Seebeck and Nernst effects associated with the nonrelativistic component of the nondegenerate spin-wave dispersion in altermagnets, in the particular case of RuO_2, chosen here as a reference example for altermagnets. Our conclusions also apply, qualitatively, to other materials with alike unit-cell geometry and magnetic order, such as, e.g., MnF_2, FeF_2, CoF_2, and to cases with more than two sublattices with antiparallel magnetic moments and/or with a different than fourfold rotation symmetry, e.g., Fe_3O_4 or MnTe.

Since the sign and spatial profile of the spin accumulation generated by the emergent magnon currents are fundamentally linked to the altermagnetic spin-group symmetry, we propose that experimental detection of the ensuing spin accumulation, e.g., by magneto-optical measurements, could be a feasible method for an indirect identification of materials, particularly insulators, as altermagnetic.

ACKNOWLEDGMENTS

The authors thank S. Mankovsky for valuable discussions. M.W. acknowledges financial support from the German Research Foundation (Deutsche Forschungsgemeinschaft) through CRC/TRR 227 "Ultrafast Spin Dynamics". A.M. acknowledges partial financial support from the Czech Science Foundation (GA CR) Grant No. 23-04746S, and from a "long-term conceptual development of a research organization" (DKRVO) grant from the University of West Bohemia in Plzen. The computations were enabled by resources provided by the National Academic Infrastructure for Supercomputing in Sweden (NAISS) at NSC Linköping partially funded by the Swedish Research Council through Grant Agreement No. 2022-06725.

APPENDIX A: CALCULATION OF MAGNON DISPERSION IN ALTERMAGNETS

In this Appendix we derive the magnon band structure for a general altermagnet using second quantization. We start from a two-sublattice Heisenberg Hamiltonian,

$$\hat{\mathcal{H}} = -\frac{1}{S^2}\sum_{ij}\sum_{ss'} J_{ij}^{ss'}\,\hat{\mathbf{s}}_{is}\cdot\hat{\mathbf{s}}_{js'}, \tag{A1}$$

with $\hat{\mathbf{s}}_{is}$ denoting spin operators with spin quantum number S and $J_{ij}^{ss'}$ the (scalar) exchange coupling between the magnetic moments for the atoms respectively at $\boldsymbol{r}_i + \boldsymbol{b}_s$ and at $\boldsymbol{r}_j + \boldsymbol{b}_{s'}$, where $\boldsymbol{r}_i$ ($\boldsymbol{r}_j$) is the location of the unit cell within a periodic lattice, and $\boldsymbol{b}_s$ ($\boldsymbol{b}_{s'}$) the sublattice position within it.

We follow the usual scheme for the derivation of an antiferromagnetic magnon dispersion relation based on the Holstein-Primakoff transformation [57], which up to second order in magnon variables is given by

$$\hat{s}^+_{i\mathrm{a}} \approx \sqrt{2S}\hat{a}_i, \quad \hat{s}^-_{i\mathrm{a}} \approx \sqrt{2S}\hat{a}^\dagger_i, \quad \hat{s}^z_{i\mathrm{a}} = S - \hat{a}^\dagger_i\hat{a}_i,$$
$$\hat{s}^+_{i\mathrm{b}} \approx \sqrt{2S}\hat{b}^\dagger_i, \quad \hat{s}^-_{i\mathrm{b}} \approx \sqrt{2S}\hat{b}_i, \quad \hat{s}^z_{i\mathrm{b}} = -S + \hat{b}^\dagger_i\hat{b}_i, \tag{A2}$$

with $\hat{s}^\pm_{is} = \hat{s}^x_{is} \pm i\hat{s}^y_{is}$, and the magnon creation $(\hat{a}^\dagger_i, \hat{b}^\dagger_i)$ and annihilation operators $(\hat{a}_i, \hat{b}_i)$.

Inserting into the Hamiltonian (A1) and Fourier transformation (with $\hat{a}^{(\dagger)}_i = \sqrt{1/N}\sum_{\boldsymbol{k}} \exp(-i\boldsymbol{k}\cdot\boldsymbol{r}_i)\hat{a}^{(\dagger)}_{\boldsymbol{k}}$ and analogous for $\hat{b}^{(\dagger)}_i$) yields $\hat{\mathcal{H}} \approx \text{const.} + \hat{\mathcal{H}}^{\mathrm{mag}}$, with

$$\hat{\mathcal{H}}^{\mathrm{mag}} = \sum_{\boldsymbol{k}} (\hat{a}^\dagger_{\boldsymbol{k}} \quad \hat{b}_{\boldsymbol{k}}) \mathcal{H}_{\boldsymbol{k}} \begin{pmatrix} \hat{a}_{\boldsymbol{k}} \\ \hat{b}^\dagger_{\boldsymbol{k}} \end{pmatrix}, \tag{A3}$$

$$\mathcal{H}_{\boldsymbol{k}} = -\frac{2}{S}\begin{pmatrix} \tilde{J}^{\mathrm{aa}}_{\boldsymbol{k}} - \tilde{J}^{\mathrm{aa}}_{\boldsymbol{0}} + \tilde{J}^{\mathrm{ab}}_{\boldsymbol{0}} & \tilde{J}^{\mathrm{ab}}_{\boldsymbol{k}} \\ \tilde{J}^{\mathrm{ab}}_{\boldsymbol{k}} & \tilde{J}^{\mathrm{bb}}_{\boldsymbol{k}} - \tilde{J}^{\mathrm{bb}}_{\boldsymbol{0}} + \tilde{J}^{\mathrm{ab}}_{\boldsymbol{0}} \end{pmatrix}. \tag{A4}$$

Note that we have introduced the Fourier transformed exchange coupling constants $\tilde{J}^{ss'}_{\boldsymbol{k}} = \sum_j \exp(i\boldsymbol{k}\cdot\boldsymbol{r}_j) J^{ss'}_{ij}$.

Next, we perform a bosonic Bogoliubov-Valatin transformation [58,59] to diagonalize the Hamiltonian. We introduce new magnon variables $(\hat{\alpha}^{(\dagger)}_{\boldsymbol{k}}, \hat{\beta}^{(\dagger)}_{\boldsymbol{k}})$ via

$$\hat{a}_{\boldsymbol{k}} = u_{\boldsymbol{k}}\hat{\alpha}_{\boldsymbol{k}} - v_{\boldsymbol{k}}\hat{\beta}^\dagger_{\boldsymbol{k}}, \tag{A5}$$

$$\hat{b}^\dagger_{\boldsymbol{k}} = u_{\boldsymbol{k}}\hat{\beta}^\dagger_{\boldsymbol{k}} - v_{\boldsymbol{k}}\hat{\alpha}_{\boldsymbol{k}}, \tag{A6}$$

where the real coefficients $u_{\boldsymbol{k}}$ and $v_{\boldsymbol{k}}$ fulfill $u^2_{\boldsymbol{k}} - v^2_{\boldsymbol{k}} = 1$ in order to conserve the canonical commutation relations. From this we get the diagonalized magnon Hamiltonian

$$\hat{\mathcal{H}}^{\mathrm{mag}} = \sum_{\boldsymbol{k}} \hbar\omega^\alpha_{\boldsymbol{k}}\hat{\alpha}^\dagger_{\boldsymbol{k}}\hat{\alpha}_{\boldsymbol{k}} + \hbar\omega^\beta_{\boldsymbol{k}}\hat{\beta}^\dagger_{\boldsymbol{k}}\hat{\beta}_{\boldsymbol{k}} \tag{A7}$$

with the magnon frequencies

$$\omega^\alpha_{\boldsymbol{k}} = \frac{\omega^{\mathrm{a}}_{\boldsymbol{k}} - \omega^{\mathrm{b}}_{\boldsymbol{k}}}{2} + \sqrt{\left(\frac{\omega^{\mathrm{a}}_{\boldsymbol{k}} + \omega^{\mathrm{b}}_{\boldsymbol{k}}}{2} - \frac{S\tilde{J}^{\mathrm{ab}}_{\boldsymbol{0}}}{\hbar}\right)^2 - \left(\frac{S\tilde{J}^{\mathrm{ab}}_{\boldsymbol{k}}}{\hbar}\right)^2}, \tag{A8}$$

$$\omega^\beta_{\boldsymbol{k}} = \frac{\omega^{\mathrm{a}}_{\boldsymbol{k}} - \omega^{\mathrm{b}}_{\boldsymbol{k}}}{2} - \sqrt{\left(\frac{\omega^{\mathrm{a}}_{\boldsymbol{k}} + \omega^{\mathrm{b}}_{\boldsymbol{k}}}{2} - \frac{S\tilde{J}^{\mathrm{ab}}_{\boldsymbol{0}}}{\hbar}\right)^2 - \left(\frac{S\tilde{J}^{\mathrm{ab}}_{\boldsymbol{k}}}{\hbar}\right)^2}. \tag{A9}$$

Here, we introduced $\omega^a_{\boldsymbol{k}} = 2(\tilde{J}^{\mathrm{aa}}_{\boldsymbol{0}} - \tilde{J}^{\mathrm{aa}}_{\boldsymbol{k}})/(S\hbar)$ and $\omega^b_{\boldsymbol{k}} = 2(\tilde{J}^{\mathrm{bb}}_{\boldsymbol{0}} - \tilde{J}^{\mathrm{bb}}_{\boldsymbol{k}})/(S\hbar)$. For zero intersublattice coupling one recovers two decoupled ferromagnetic dispersion relations $\omega^\alpha_{\boldsymbol{k}} = \omega^{\mathrm{a}}_{\boldsymbol{k}}$ and $\omega^\beta_{\boldsymbol{k}} = \omega^{\mathrm{b}}_{\boldsymbol{k}}$, which are separately hosted on the distinct sublattices. Similarly, the magnon frequencies reduce to the typical antiferromagnetic magnon dispersion relation $\omega^\alpha_{\boldsymbol{k}} = 2\sqrt{(\tilde{J}^{\mathrm{ab}}_{\boldsymbol{0}})^2 - (\tilde{J}^{\mathrm{ab}}_{\boldsymbol{k}})^2/(S\hbar)}$ and $\omega^\beta_{\boldsymbol{k}} = -2\sqrt{(\tilde{J}^{\mathrm{ab}}_{\boldsymbol{0}})^2 - (\tilde{J}^{\mathrm{ab}}_{\boldsymbol{k}})^2/(S\hbar)}$ in the absence of intrasublattice coupling. The magnon eigenmodes for RuO_2 are depicted in Fig. 2(b).

Unlike the magnons in the original $(\hat{a}^{(\dagger)}_{\boldsymbol{k}}, \hat{b}^{(\dagger)}_{\boldsymbol{k}})$ basis, which only have a finite amplitude at one of the sublattices, the magnons in the new $(\hat{\alpha}^{(\dagger)}_{\boldsymbol{k}}, \hat{\beta}^{(\dagger)}_{\boldsymbol{k}})$ basis are characterized by a tilting of the moments in both sublattices,

$$\begin{aligned}\Delta\hat{s}^z_{\mathrm{a}} &= \sum_i S - \hat{S}^z_{i\mathrm{a}} \\ &= \sum_{\boldsymbol{k}} u^2_{\boldsymbol{k}}\hat{\alpha}^\dagger_{\boldsymbol{k}}\hat{\alpha}_{\boldsymbol{k}} + v^2_{\boldsymbol{k}}(\hat{\beta}^\dagger_{\boldsymbol{k}}\hat{\beta}_{\boldsymbol{k}} + 1) \\ &\quad - u_{\boldsymbol{k}}v_{\boldsymbol{k}}(\hat{\alpha}^\dagger_{\boldsymbol{k}}\hat{\beta}^\dagger_{\boldsymbol{k}} + \hat{\alpha}_{\boldsymbol{k}}\hat{\beta}_{\boldsymbol{k}}),\end{aligned} \tag{A10}$$

$$\begin{aligned}\Delta\hat{s}^z_{\mathrm{b}} &= \sum_i S + \hat{S}^z_{i\mathrm{b}} \\ &= \sum_{\boldsymbol{k}} u^2_{\boldsymbol{k}}\hat{\beta}^\dagger_{\boldsymbol{k}}\hat{\beta}_{\boldsymbol{k}} + v^2_{\boldsymbol{k}}(\hat{\alpha}^\dagger_{\boldsymbol{k}}\hat{\alpha}_{\boldsymbol{k}} + 1) \\ &\quad - u_{\boldsymbol{k}}v_{\boldsymbol{k}}(\hat{\alpha}^\dagger_{\boldsymbol{k}}\hat{\beta}^\dagger_{\boldsymbol{k}} + \hat{\alpha}_{\boldsymbol{k}}\hat{\beta}_{\boldsymbol{k}}).\end{aligned} \tag{A11}$$

From that we get that the sublattice amplitudes for the α magnon branch are $\langle 0|\hat{\alpha}_{\boldsymbol{k}}\Delta\hat{s}^z_a\hat{\alpha}^\dagger_{\boldsymbol{k}}|0\rangle = u^2_{\boldsymbol{k}} + v^2_{\boldsymbol{k}}$ and $\langle 0|\hat{\alpha}_{\boldsymbol{k}}\Delta\hat{s}^z_b\hat{\alpha}^\dagger_{\boldsymbol{k}}|0\rangle = 2v^2_{\boldsymbol{k}}$, while for the β magnon branch they are $\langle 0|\hat{\beta}_{\boldsymbol{k}}\Delta\hat{s}^z_a\hat{\beta}^\dagger_{\boldsymbol{k}}|0\rangle = 2v^2_{\boldsymbol{k}}$ and $\langle 0|\hat{\beta}_{\boldsymbol{k}}\Delta\hat{s}^z_b\hat{\beta}^\dagger_{\boldsymbol{k}}|0\rangle = u^2_{\boldsymbol{k}} + v^2_{\boldsymbol{k}}$. Here, $|0\rangle$ denotes the ground state of the system. Henceforth, the ratio $R_{\boldsymbol{k}}$ of the respective smaller and larger magnon amplitude at each sublattice is given by $R_{\boldsymbol{k}} = 2v^2_{\boldsymbol{k}}/(u^2_{\boldsymbol{k}} + v^2_{\boldsymbol{k}}) = 2v^2_{\boldsymbol{k}}/(1 + 2v^2_{\boldsymbol{k}}) \leqslant 1$. This quantity calculated for the case of RuO_2 is shown in Fig. 2(c).

The operator for the total z magnetization in the new basis set is given by the difference in magnon numbers in each branch before and after the Bogoliubov-Valatin transformation,

$$\hat{s}^z = \sum_i \hat{S}^z_{ia} + \hat{S}^z_{ib} = \sum_{\boldsymbol{k}} \hat{b}^\dagger_{\boldsymbol{k}}\hat{b}_{\boldsymbol{k}} - \hat{a}^\dagger_{\boldsymbol{k}}\hat{a}_{\boldsymbol{k}} = \sum_{\boldsymbol{k}} \hat{\beta}^\dagger_{\boldsymbol{k}}\hat{\beta}_{\boldsymbol{k}} - \hat{\alpha}^\dagger_{\boldsymbol{k}}\hat{\alpha}_{\boldsymbol{k}}. \tag{A12}$$

Consequently, the α and β magnons carry opposite spin angular momentum along the z-direction, since $\langle 0|\hat{\alpha}_{\boldsymbol{k}}\hat{s}^z\hat{\alpha}^\dagger_{\boldsymbol{k}}|0\rangle = -1$ and $\langle 0|\hat{\beta}_{\boldsymbol{k}}\hat{s}^z\hat{\beta}^\dagger_{\boldsymbol{k}}|0\rangle = 1$.

APPENDIX B: BOLTZMANN TRANSPORT THEORY FOR MAGNON CURRENTS AND SPIN ACCUMULATION

Within our approach, the z component of the magnetization $S^z = \langle\hat{s}^z\rangle$ is given by the difference of the total magnon numbers in each branch,

$$S^z = \sum_{\boldsymbol{k}} \langle\hat{\beta}^\dagger_{\boldsymbol{k}}\hat{\beta}_{\boldsymbol{k}}\rangle - \langle\hat{\alpha}^\dagger_{\boldsymbol{k}}\hat{\alpha}_{\boldsymbol{k}}\rangle = \sum_{\boldsymbol{k}} n^\beta_{\boldsymbol{k}} - n^\alpha_{\boldsymbol{k}}. \tag{B1}$$

To describe spatially nonhomogeneous and possibly time-dependent magnon occupations, we use Boltzmann equations within the relaxation time ansatz,

$$\frac{\partial n^\sigma_{\boldsymbol{k}}(\boldsymbol{r},t)}{\partial t} + \frac{\partial n^\sigma_{\boldsymbol{k}}(\boldsymbol{r},t)}{\partial \boldsymbol{r}} \cdot \frac{\partial\omega^\sigma_{\boldsymbol{k}}}{\partial\boldsymbol{k}} = -\frac{n^\sigma_{\boldsymbol{k}}(\boldsymbol{r},t) - f^\sigma_{\boldsymbol{k}}(\boldsymbol{r},t)}{\tau^\sigma_{\boldsymbol{k}}}, \tag{B2}$$

with $\sigma \in [\alpha, \beta]$. Here, $\partial\omega^\sigma_{\boldsymbol{k}}/\partial\boldsymbol{k} = \boldsymbol{v}_{\boldsymbol{k}}$ and $\tau^\sigma_{\boldsymbol{k}}$ are the branch- and $\boldsymbol{k}$-dependent magnon velocities and lifetimes, respectively, and $f^\sigma_{\boldsymbol{k}}(\boldsymbol{r},t)$ is the equilibrium magnon occupation.

In steady state and for the current along the x direction, we get that

$$\frac{\partial n^\sigma_{\boldsymbol{k}}(x)}{\partial x} = -\frac{n^\sigma_{\boldsymbol{k}}(x) - f^\sigma_{\boldsymbol{k}}(x)}{v^\sigma_{\boldsymbol{k}}\tau^\sigma_{\boldsymbol{k}}}. \tag{B3}$$

Hereinafter, we solve this equation for the case of a temperature step at $x = 0$ that connects two regions of constant temperature. In this case, we have a constant equilibrium magnon occupations $f_{\boldsymbol{k}}^{\sigma}(x < 0) = c_{\boldsymbol{k}}^{\sigma}$ and $f_{\boldsymbol{k}}^{\sigma}(x \geqslant 0) = d_{\boldsymbol{k}}^{\sigma}$ in the two regions. A simple calculation yields that the occupation number of any magnon with $v > 0$ has the solution

$$n_{\boldsymbol{k}}^{\sigma,v>0}(x) = \begin{cases} c_{\boldsymbol{k}}^{\sigma} & \text{for } x < 0 \\ (c_{\boldsymbol{k}}^{\sigma} - d_{\boldsymbol{k}}^{\sigma}) e^{-x/(v_{\boldsymbol{k}}^{\sigma}\tau_{\boldsymbol{k}}^{\sigma})} + d_{\boldsymbol{k}}^{\sigma} & \text{for } x \geqslant 0 \end{cases} \tag{B4}$$

and, analogously, the occupation number of magnons with $v < 0$ follows

$$n_{\boldsymbol{k}}^{\sigma,v<0}(x) = \begin{cases} (d_{\boldsymbol{k}}^{\sigma} - c_{\boldsymbol{k}}^{\sigma}) e^{-x/(v_{\boldsymbol{k}}^{\sigma}\tau_{\boldsymbol{k}}^{\sigma})} + c_{\boldsymbol{k}}^{\sigma} & \text{for } x < 0 \\ d_{\boldsymbol{k}}^{\sigma} & \text{for } x \geqslant 0. \end{cases} \tag{B5}$$

To simplify the following calculations we assume that $T(x > 0)$ is zero, which implies that $d_{\boldsymbol{k}}^{\sigma} = 0$, and compute the solution only in the region $x > 0$. Inserting into Eq. (B1) yields

$$\begin{aligned} S^z(x > 0) &= \sum_{\boldsymbol{k}} n_{\boldsymbol{k}}^{\beta,v>0}(x) - n_{\boldsymbol{k}}^{\alpha,v>0}(x) \\ &= \sum_{\boldsymbol{k}} c_{\boldsymbol{k}}^{\beta} e^{-x/\lambda_{\boldsymbol{k}}^{\beta}} - c_{\boldsymbol{k}}^{\alpha} e^{-x/\lambda_{\boldsymbol{k}}^{\alpha}}, \end{aligned} \tag{B6}$$

where the decay length $\lambda_{\boldsymbol{k}}^{\sigma} = v_{\boldsymbol{k}}^{\beta}\tau_{\boldsymbol{k}}^{\beta}$ was introduced. To evaluate the above expression, it is necessary to know the lifetimes $\tau_{\boldsymbol{k}}^{\sigma}$ of the magnon modes. Following Ref. [18], we apply a constant lifetime approximation $\tau_{\boldsymbol{k}}^{\sigma} \equiv \tau_0$. Since we want to compare with spin dynamics simulations based on the sLLG, we assume a classical equilibrium occupation $c_{\boldsymbol{k}}^{\sigma} = k_{\mathrm{B}}T/(\hbar\omega_{\boldsymbol{k}}^{\sigma})$ [60], rather than a Bose-Einstein distribution. The result for the emergent magnetization for different orientations of the temperature step is shown in Fig. 9(a) and agrees qualitatively very well with what we obtained via simulations (see Sec. III).

Summation over $\boldsymbol{k}$ transforms Eq. (B2) to the respective continuity equations for each magnon branch,

$$\frac{\partial}{\partial t} N_{\sigma}(\boldsymbol{r}, t) + \nabla \cdot \boldsymbol{j}_{\sigma}(\boldsymbol{r}, t) = -\Gamma_{\sigma}(\boldsymbol{r}, t), \tag{B7}$$

where $N_{\sigma}(\boldsymbol{r}, t) = \sum_{\boldsymbol{k}} n_{\boldsymbol{k}}^{\sigma}(\boldsymbol{r}, t)$ is the total magnon number in each branch, $\boldsymbol{j}_{\sigma}(\boldsymbol{r}, t) = \sum_{\boldsymbol{k}} n_{\boldsymbol{k}}^{\sigma}(\boldsymbol{r}, t)\boldsymbol{v}_{\boldsymbol{k}}^{\sigma}$ is the magnon current carrying z-component spin angular momentum and $\Gamma_{\sigma}(\boldsymbol{r}, t) = (N_{\sigma}(\boldsymbol{r}, t) - N^0(\boldsymbol{r}, t))/\tau_0$ is a sink term. Note that the total number of magnons in the equilibrium $N^0(\boldsymbol{r}, t)$ is the same for both magnon branches because of the summation over the entire Brillouin zone.

Recalling that the z magnetization is determined by the difference between the respective magnon numbers in each branch [cf. Eq. (B1)] we subtract the continuity equation for the α branch from the one for the β branch, yielding

$$\begin{aligned} &\frac{\partial}{\partial t}(N_{\beta}(\boldsymbol{r}, t) - N_{\alpha}(\boldsymbol{r}, t)) + \nabla \cdot (\boldsymbol{j}_{\beta}(\boldsymbol{r}, t) - \boldsymbol{j}_{\alpha}(\boldsymbol{r}, t)) \\ &\quad = -\frac{N_{\beta}(\boldsymbol{r}, t) - N_{\alpha}(\boldsymbol{r}, t)}{\tau_0}. \end{aligned} \tag{B8}$$

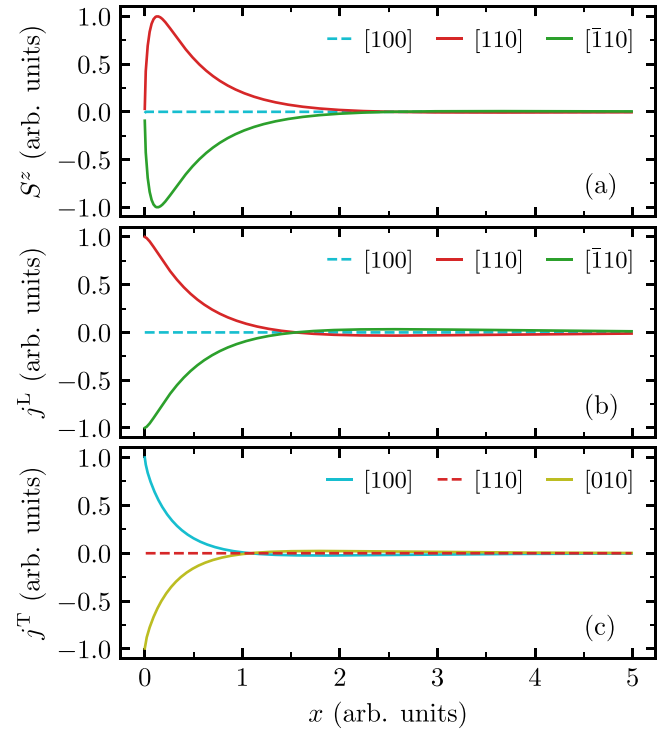

FIG. 9. Spin Seebeck and spin Nernst effect in altermagnetic RuO_2 induced by a temperature step at $x = 0$ calculated by Boltzmann transport theory. Spin accumulation S^z (a), longitudinal spin current (b), and transverse spin current (c) are shown versus position coordinate for different crystallographic directions (color coded).

By that, we arrive at the continuity equation of the emergent magnetization

$$\frac{\partial S^z(\boldsymbol{r}, t)}{\partial t} + \nabla \cdot \boldsymbol{j}(\boldsymbol{r}, t) = -\frac{S^z(\boldsymbol{r}, t)}{\tau_0}, \tag{B9}$$

where we introduced the spin current as

$$\boldsymbol{j}(\boldsymbol{r}, t) = \sum_{\boldsymbol{k}} n_{\boldsymbol{k}}^{\beta}(\boldsymbol{r}, t)\boldsymbol{v}_{\boldsymbol{k}}^{\beta} - n_{\boldsymbol{k}}^{\alpha}(\boldsymbol{r}, t)\boldsymbol{v}_{\boldsymbol{k}}^{\alpha}. \tag{B10}$$

Unsurprisingly, it is given by the sum of the magnon currents $\boldsymbol{j}_{\mathrm{s}}^{\sigma}(\boldsymbol{r}, t) = \sum_{\boldsymbol{k}} n_{\boldsymbol{k}}^{\sigma}(\boldsymbol{r}, t)\boldsymbol{v}_{\boldsymbol{k}}^{\sigma}$ of each sublattice multiplied by the respective spin angular momentum along the z direction of ± 1. In Figs. 9(b) and 9(c) we demonstrate that the longitudinal and transverse magnonic spin currents are again in good qualitative agreement with the simulation results shown in Sec. III.

For steady state $[\partial S^z(\boldsymbol{r}, t)/\partial t = 0]$, we get

$$\nabla \cdot \boldsymbol{j}(\boldsymbol{r}) = -\frac{S_z(\boldsymbol{r})}{\tau_0}. \tag{B11}$$

While we found this relation to be not exactly fulfilled in the simulations (see Sec. III)—most likely because of shortcomings of the constant lifetime approximation—it nonetheless provides a useful relation between between the magnonic spin current and the emergent magnetization.

APPENDIX C: SIMULATION METHODS

We perform atomistic spin dynamics simulations based on the stochastic Landau-Lifshitz-Gilbert (sLLG) equation of

motion for a sufficiently big ensemble of atomic magnetic moments [39–41],

$$\frac{\partial \boldsymbol{S}_{is}}{\partial t} = -\frac{\gamma}{(1+\alpha^2)\mu_s}\boldsymbol{S}_{is} \times (\boldsymbol{H}_{is} + \alpha \boldsymbol{S}_{is} \times \boldsymbol{H}_{is}). \tag{C1}$$

Here $\boldsymbol{S}_{is}$ denotes a unit vector in the direction of the Ru magnetic moment of sublattice s in the unit cell i, α is the Gilbert damping parameter, μ_s is the saturation magnetic moment, and γ is the gyromagnetic ratio.

This numerical approach goes beyond noninteracting spin-wave theory, as used in previous studies such as, e.g., Ref. [17,18], and may provide a more realistic description of experiments [61] in terms of adiabatic magnon dispersion. On the other hand, it neglects intrinsic damping effects because of the Stoner continuum, which can be large in metallic magnetic materials and would show up as a possibly shifted position of the peaks associated with magnon dispersion, and their their progressively broader FWHM, particularly toward the boundary of the Brillouin zone. Within the framework of the sLLG, damping is included via the Gilbert term (proportional to the Gilbert damping parameter α), because of which each individual atomic magnetic moment tends to gradually spiral back toward its ground state direction.

Since we are only interested in steady-state solutions of the sLLG, we can set $\mu_s = \gamma = 1$. To the best of our knowledge, the Gilbert damping parameter for RuO_2 is unknown. That is why we choose an intermediate value of $\alpha = 0.001$ for the simulations presented in Sec. III. We have also performed simulations with $\alpha = 0.01$ (not shown) and found that this only affects the magnitude and length scale of the resulting effects, while they are qualitatively the same. The effective field $\boldsymbol{H}_{is} = -\partial\mathcal{H}/\partial\boldsymbol{S}_{is} + \boldsymbol{\zeta}_{is}$ contains both a deterministic field that stems from the spin Hamiltonian (1) and a stochastic field $\boldsymbol{\zeta}_{is}$ in the form of Gaussian white noise [62],

$$\langle \boldsymbol{\zeta}_{is} \rangle = 0, \tag{C2}$$

$$\langle \boldsymbol{\zeta}_{\mathrm{is}}(t)(\boldsymbol{\zeta}_{\mathrm{is}}(0))^{\mathrm{T}} \rangle = 2\frac{\alpha k_B T_i \mu_s}{\gamma}\delta_{ij}\delta_{ss'}\delta(t)\mathbb{1}, \tag{C3}$$

which models a coupling to a heat bath—incorporating the interaction of localized spins with electronic and phononic degrees of freedom—with a local temperature T_i. The numerical integration of the sLLG is carried out using the Heun algorithm [41]. To reduce the computational cost we introduce an energy cutoff for the Heisenberg exchange constants such that only those with $|J_{ij}^{ss'}| \geqslant 0.0625\,\mathrm{meV}$ are included. By calculating the Néel order parameter $L = \frac{1}{2N}|\sum_i^N \boldsymbol{S}_{ia} - \boldsymbol{S}_{ib}|$, with N being the number of unit cells and a and b denoting the Ru respective sublattices, versus temperature we estimate a critical temperature of $T_c \approx 125\,\mathrm{K}$ (see Fig. 10). In our simulations of the magnon currents and the emergent magnetization we consider a system extended in the direction of the temperature step/gradient consisting of $36 \times 36 \times 1600$ unit cells (equalling to 4 147 200 Ru moments). Moreover, we apply periodic boundary conditions in the directions perpendicular to the temperature step/gradient to eliminate finite-size effects.

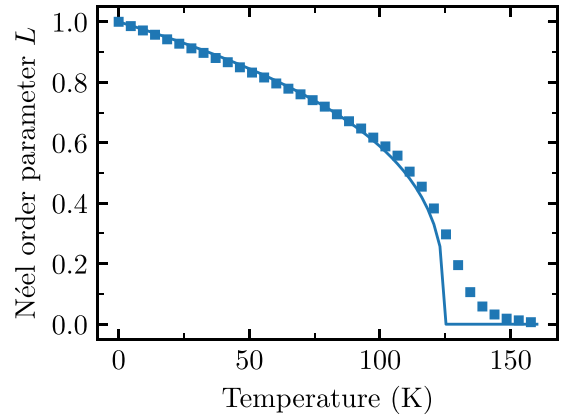

FIG. 10. Néel order parameter L of altermagnetic RuO_2 for a system consisting of 128 000 Ru moments calculated using the sLLG and spin model parameters from Ref. [17]. The simulation results are fitted to the expression $L(T) = (1 - T/T_c)^{0.33}$ (shown as solid line), which yields a fitted $T_c \approx 125\,\mathrm{K}$.

APPENDIX D: NUMERICAL CALCULATION OF SPIN CURRENTS IN ATOMISTIC SPIN DYNAMICS SIMULATIONS

When doing magnon transport calculations, theoretical models based on linear response theory and Boltzmann transport theory typically only compute the spin current, rather than the associated magnetization dynamics. Atomistic spin dynamics simulations, on the other hand, are used to directly calculate the temporal evolution of the magnetic moments, which only indirectly contains information about the spin currents via a possibly arising spin accumulation. To bridge this gap, earlier studies introduced formulas to obtain the spin currents in ferromagnets within continuum theory [1] and atomistic descriptions including only isotropic nearest-neighbor Heisenberg exchange [51]. Hereinafter, we derive an expression to calculate the spin current for multisublattice systems such as, e.g., antiferro- and altermagnets, with arbitrary Heisenberg exchange interaction extending beyond nearest neighbors.

Neglecting losses caused by Gilbert damping, the time-averaged change of spin in a single unit cell with index i follows from the Landau-Lifshitz-Gilbert equation as

$$\left\langle \sum_s \dot{\boldsymbol{S}}_{is} \right\rangle = -\frac{\gamma}{\mu_s}\sum_{ss',\delta} J_{i,i+\delta}^{ss'} \langle \boldsymbol{S}_{is} \times \boldsymbol{S}_{i+\delta,s'} \rangle, \tag{D1}$$

with s, s' being the sublattice indices. For simplicity, we consider only a 1D chain of unit cells. Generalization to 3D systems, however, is straightforward. The right-hand side of Eq. (D1) can be viewed as the difference between incoming ($\delta < 0$) and outgoing ($\delta > 0$) spin momentum. Note that the terms for $\delta = 0$, i.e., within the chosen unit cell, mutually cancel because of the antisymmetry of the cross product. Thus, we can write a discretized continuity equation, $\langle \sum_s \dot{\boldsymbol{S}}_{is} \rangle = -(\boldsymbol{j}_i^{\mathrm{in}} - \boldsymbol{j}_i^{\mathrm{out}})/d$, with the incoming and outgoing spin currents

$$\boldsymbol{j}_i^{\mathrm{in}} = \frac{\gamma}{\mu_s} d \sum_{ss',\delta<0} J_{i,i+\delta}^{ss'} \langle \boldsymbol{S}_{is} \times \boldsymbol{S}_{i+\delta,s'} \rangle, \tag{D2}$$

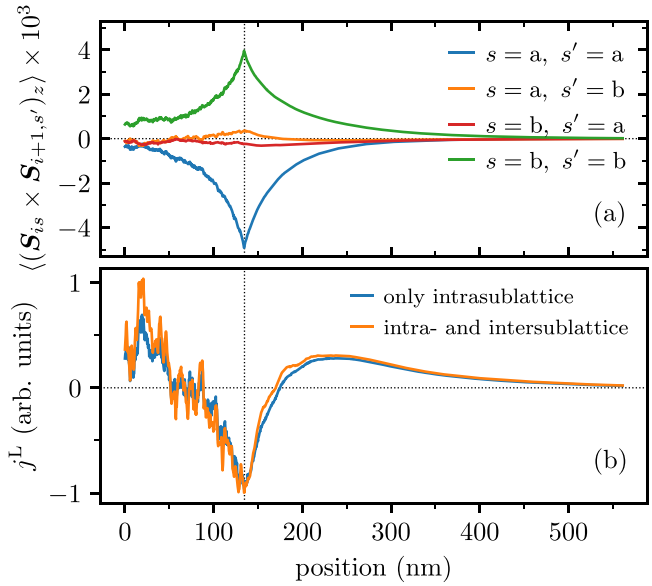

FIG. 11. (a) Intra- ($s = s'$) and intersublattice ($s \neq s'$) correlations for a temperature step with $T = 10\,\mathrm{K}$ to the left of the vertical-dotted line and zero to the right. (b) Spatial profile of the z component of the longitudinal spin current calculated considering only intrasublattice correlations and both intra- and intersublattice correlations with the next unit cell. Note that the resulting curves have been scaled to the same magnitude.

$$\boldsymbol{j}_i^{\mathrm{out}} = -\frac{\gamma}{\mu_{\mathrm{s}}} d \sum_{ss',\delta>0} J_{i,i+\delta}^{ss'} \langle \boldsymbol{S}_{is} \times \boldsymbol{S}_{i+\delta,s'} \rangle. \tag{D3}$$

In steady state (for which $\langle \sum_s \dot{\boldsymbol{S}}_{is} \rangle = 0$) incoming and outgoing currents are equal, $\boldsymbol{j}_i^{\mathrm{in}} = \boldsymbol{j}_i^{\mathrm{out}} := \boldsymbol{j}_i$, and henceforth either of the expressions above can be used to calculate the spin current $\boldsymbol{j}_i$ for arbitrary $J_{ij}^{ss'}$ and ground-state configuration.

When applying this method to obtain the spin currents from our simulations on RuO_2, we consider only the spin transport to the respective nearest unit cells to simplify the calculations. As demonstrated in Fig. 11(a), the intrasublattice correlations turn out to be much larger than the intersublattice correlations, i.e., $\langle \boldsymbol{S}_{is} \times \boldsymbol{S}_{i\pm1,s'=s} \rangle \gg \langle \boldsymbol{S}_{is} \times \boldsymbol{S}_{i\pm1,s'\neq s} \rangle$. This is because of the fact that only in the vicinity of the Γ point of the Brillouin zone the magnon excitations involve both sublattices while they are primarily hosted by only one of them at the rest of the Brillouin zone.

Henceforth, we use the following expression for estimating spin currents in RuO2:

$$\boldsymbol{j}_i \approx -\frac{\gamma}{\mu_{\mathrm{s}}} A_{\mathrm{lat}} J (\langle \boldsymbol{S}_{i\mathrm{a}} \times \boldsymbol{S}_{i+1,\mathrm{a}} \rangle + \langle \boldsymbol{S}_{i\mathrm{b}} \times \boldsymbol{S}_{i+1,\mathrm{b}} \rangle), \tag{D4}$$

where we have introduced $J := J_{i,i+1}^{\mathrm{aa}} = J_{i,i+1}^{\mathrm{bb}}$. We checked in Fig. 11(b) that neglecting intersublattice correlations indeed has no qualitative impact on the spin current profile.

APPENDIX E: HEISENBERG EXCHANGE PARAMETERS

The exchange parameters for the Heisenberg Hamiltonian (1) were obtained from density functional theory in the spin-polarized relativistic Korringa-Kohn-Rostoker implementation [63]. We use the local spin density approximation in the Vosko-Wilk-Nusair parametrization [64] and the DFT+U procedure with the rotationally invariant approach of Dudarev *et al.* [65], to improve the description of Ru d orbitals responsible for the finite magnetic moments. The results for the electronic structure were calculated by solving the Kohn-Sham equation in its fully relativistic formulation [66].

The exchange constants between Ru magnetic moments at relative position $\boldsymbol{R}_{ij}^{ss'} = \boldsymbol{r}_j - \boldsymbol{r}_i + \boldsymbol{b}_{s'} - \boldsymbol{b}_s$, with $\boldsymbol{r}_{i(j)}$ being the location of the unit cell within the lattice and $\boldsymbol{b}_{s(s')}$ the sublattice position within the unit cell, are listed in Table I.

TABLE I. Cartesian components of $\boldsymbol{R}_{ij}^{ss'}$ in Å and Heisenberg exchange constants $J_{ij}^{ss'}$ in meV for $s = 1$. The exchange constants for $s = 2$ can be obtained using the crystal symmetry.

$X_{ij}^{ss'}$	$Y_{ij}^{ss'}$	$Z_{ij}^{ss'}$	$J_{ij}^{ss'}$	$X_{ij}^{ss'}$	$Y_{ij}^{ss'}$	$Z_{ij}^{ss'}$	$J_{ij}^{ss'}$
0.000	0.000	3.106	1.8659	4.493	−8.986	0.000	0.0667
0.000	0.000	−3.106	1.8659	8.986	−4.493	0.000	0.0667
2.247	−2.247	1.553	−2.6739	−8.986	4.493	0.000	0.0667
−2.247	−2.247	1.553	−2.6739	−4.493	8.986	0.000	0.0667
2.247	2.247	1.553	−2.6739	0.000	−4.493	9.318	0.0738
−2.247	2.247	1.553	−2.6739	4.493	0.000	9.318	0.0738
2.247	−2.247	−1.553	−2.6739	−4.493	0.000	9.318	0.0738
−2.247	−2.247	−1.553	−2.6739	0.000	4.493	9.318	0.0738
2.247	2.247	−1.553	−2.6739	0.000	−4.493	−9.318	0.0738
−2.247	2.247	−1.553	−2.6739	4.493	0.000	−9.318	0.0738
0.000	−4.493	0.000	0.1185	−4.493	0.000	−9.318	0.0738
4.493	0.000	0.000	0.1185	0.000	4.493	−9.318	0.0738
−4.493	0.000	0.000	0.1185	4.493	−8.986	3.106	0.0707
0.000	4.493	0.000	0.1185	8.986	−4.493	3.106	0.0707
2.247	−2.247	4.659	−0.3963	−8.986	4.493	3.106	0.0707
−2.247	−2.247	4.659	−0.3963	−4.493	8.986	3.106	0.0707

TABLE I. *(Continued.)*

$X_{ij}^{ss'}$	$Y_{ij}^{ss'}$	$Z_{ij}^{ss'}$	$J_{ij}^{ss'}$	$X_{ij}^{ss'}$	$Y_{ij}^{ss'}$	$Z_{ij}^{ss'}$	$J_{ij}^{ss'}$
2.247	2.247	4.659	−0.3963	4.493	−8.986	−3.106	0.0707
−2.247	2.247	4.659	−0.3963	8.986	−4.493	−3.106	0.0707
2.247	−2.247	−4.659	−0.3963	−8.986	4.493	−3.106	0.0707
−2.247	−2.247	−4.659	−0.3963	−4.493	8.986	−3.106	0.0707
2.247	2.247	−4.659	−0.3963	−4.493	−4.493	9.318	0.2732
−2.247	2.247	−4.659	−0.3963	4.493	4.493	9.318	0.2732
0.000	0.000	6.212	−2.1635	−4.493	−4.493	−9.318	0.2732
0.000	0.000	−6.212	−2.1635	4.493	4.493	−9.318	0.2732
4.493	−4.493	0.000	−1.2611	8.986	−8.986	0.000	−0.6292
−4.493	−4.493	0.000	0.5636	−8.986	−8.986	0.000	−0.0631
4.493	4.493	0.000	0.5636	8.986	8.986	0.000	−0.0631
−4.493	4.493	0.000	−1.2611	−8.986	8.986	0.000	−0.6292
4.493	−4.493	3.106	0.2252	8.986	−8.986	3.106	0.0721
−4.493	−4.493	3.106	−0.0897	−8.986	−8.986	3.106	−0.1845
4.493	4.493	3.106	−0.0897	8.986	8.986	3.106	−0.1845
−4.493	4.493	3.106	0.2252	−8.986	8.986	3.106	0.0721
4.493	−4.493	−3.106	0.2252	8.986	−8.986	−3.106	0.0721
−4.493	−4.493	−3.106	−0.0897	−8.986	−8.986	−3.106	−0.1845
4.493	4.493	−3.106	−0.0897	8.986	8.986	−3.106	−0.1845
−4.493	4.493	−3.106	0.2252	−8.986	8.986	−3.106	0.0721
2.247	−6.740	1.553	−0.0644	4.493	−4.493	12.424	0.2271
−2.247	−6.740	1.553	−0.0644	−4.493	4.493	12.424	0.2271
6.740	−2.247	1.553	−0.0644	4.493	−4.493	−12.424	0.2271
−6.740	−2.247	1.553	−0.0644	−4.493	4.493	−12.424	0.2271
6.740	2.247	1.553	−0.0644	8.986	−8.986	6.212	−0.1377
−6.740	2.247	1.553	−0.0644	−8.986	−8.986	6.212	−0.2474
2.247	6.740	1.553	−0.0644	8.986	8.986	6.212	−0.2474
−2.247	6.740	1.553	−0.0644	−8.986	8.986	6.212	−0.1377
2.247	−6.740	−1.553	−0.0644	8.986	−8.986	−6.212	−0.1377
−2.247	−6.740	−1.553	−0.0644	−8.986	−8.986	−6.212	−0.2474
6.740	−2.247	−1.553	−0.0644	8.986	8.986	−6.212	−0.2474
−6.740	−2.247	−1.553	−0.0644	−8.986	8.986	−6.212	−0.1377
6.740	2.247	−1.553	−0.0644	0.000	0.000	15.530	0.2962
−6.740	2.247	−1.553	−0.0644	0.000	0.000	−15.530	0.2962
2.247	6.740	−1.553	−0.0644	8.986	−8.986	9.318	−0.1075
−2.247	6.740	−1.553	−0.0644	−8.986	8.986	9.318	−0.1075
2.247	−2.247	7.765	0.0645	8.986	−8.986	−9.318	−0.1075
−2.247	−2.247	7.765	0.0645	−8.986	8.986	−9.318	−0.1075
2.247	2.247	7.765	0.0645	0.000	0.000	18.636	0.1332
−2.247	2.247	7.765	0.0645	0.000	0.000	−18.636	0.1332
2.247	−2.247	−7.765	0.0645	13.479	−13.479	0.000	0.1164
−2.247	−2.247	−7.765	0.0645	−13.479	13.479	0.000	0.1164
2.247	2.247	−7.765	0.0645	13.479	−13.479	6.212	0.0713
−2.247	2.247	−7.765	0.0645	−13.479	13.479	6.212	0.0713
0.000	0.000	9.318	−0.7234	13.479	−13.479	−6.212	0.0713
0.000	0.000	−9.318	−0.7234	−13.479	13.479	−6.212	0.0713

[1] Y. Kajiwara, K. Harii, S. Takahashi, J. Ohe, K. Uchida, M. Mizuguchi, H. Umezawa, H. Kawai, K. Ando, K. Takanashi *et al.*, Transmission of electrical signals by spin-wave interconversion in a magnetic insulator, Nature (London) **464**, 262 (2010).

[2] G. E. W. Bauer, E. Saitoh, and B. J. van Wees, Spin caloritronics, Nat. Mater. **11**, 391 (2012).

[3] A. V. Chumak, A. A. Serga, and B. Hillebrands, Magnon transistor for all-magnon data processing, Nat. Commun. **5**, 4700 (2014).

[4] A. V. Chumak, V. I. Vasyuchka, A. A. Serga, and B. Hillebrands, Magnon spintronics, Nat. Phys. **11**, 453 (2015).

[5] L. J. Cornelissen, J. Liu, R. A. Duine, J. B. Youssef, and B. J. van Wees, Long-distance transport of magnon spin information in a magnetic insulator at room temperature, Nat. Phys. **11**, 1022 (2015).

[6] P. Pirro, V. I. Vasyuchka, A. A. Serga, and B. Hillebrands, Advances in coherent magnonics, Nat. Rev. Mater. **6**, 1114 (2021).

[7] E. V. Gomonay and V. M. Loktev, Spintronics of antiferromagnetic systems (Review Article), Low Temp. Phys. **40**, 17 (2014).

[8] O. Gomonay, V. Baltz, A. Brataas, and Y. Tserkovnyak, Antiferromagnetic spin textures and dynamics, Nat. Phys. **14**, 213 (2018).

[9] S. M. Rezende, A. Azevedo, and R. L. Rodríguez-Suárez, Introduction to antiferromagnetic magnons, J. Appl. Phys. **126**, 151101 (2019).

[10] S. M. Rezende, R. L. Rodríguez-Suárez, and A. Azevedo, Theory of the spin Seebeck effect in antiferromagnets, Phys. Rev. B **93**, 014425 (2016).

[11] J. Li, Z. Shi, V. H. Ortiz, M. Aldosary, C. Chen, V. Aji, P. Wei, and J. Shi, Spin Seebeck effect from antiferromagnetic magnons and critical spin fluctuations in epitaxial FeF_2 films, Phys. Rev. Lett. **122**, 217204 (2019).

[12] P. R. T. Ribeiro, F. L. A. Machado, M. Gamino, A. Azevedo, and S. M. Rezende, Spin Seebeck effect in antiferromagnet nickel oxide in wide ranges of temperature and magnetic field, Phys. Rev. B **99**, 094432 (2019).

[13] L. Udvardi and L. Szunyogh, Chiral asymmetry of the spin-wave spectra in ultrathin magnetic films, Phys. Rev. Lett. **102**, 207204 (2009).

[14] K. Zakeri, Y. Zhang, J. Prokop, T. H. Chuang, N. Sakr, W. X. Tang, and J. Kirschner, Asymmetric spin-wave dispersion on Fe(110): Direct evidence of the Dzyaloshinskii-Moriya interaction, Phys. Rev. Lett. **104**, 137203 (2010).

[15] L. Šmejkal, J. Sinova, and T. Jungwirth, Beyond conventional ferromagnetism and antiferromagnetism: A phase with nonrelativistic spin and crystal rotation symmetry, Phys. Rev. X **12**, 031042 (2022).

[16] L. Šmejkal, J. Sinova, and T. Jungwirth, Emerging research landscape of altermagnetism, Phys. Rev. X **12**, 040501 (2022).

[17] L. Šmejkal, A. Marmodoro, K. H. Ahn, R. González-Hernández, I. Turek, S. Mankovsky, H. Ebert, S. W. D'Souza, O. Šipr, J. Sinova, and T. Jungwirth, Chiral magnons in altermagnetic RuO_2, Phys. Rev. Lett. **131**, 256703 (2023).

[18] Q. Cui, B. Zeng, P. Cui, T. Yu, and H. Yang, Efficient spin Seebeck and spin Nernst effects of magnons in altermagnets, Phys. Rev. B **108**, L180401 (2023).

[19] S. Hayami and T. Matsumoto, Essential model parameters for nonreciprocal magnons in multisublattice systems, Phys. Rev. B **105**, 014404 (2022).

[20] C. Herring, Effect of time-reversal symmetry on energy bands of crystals, Phys. Rev. **52**, 361 (1937).

[21] V. C. Sahni and G. Venkataraman, On the application of group theory to spinwaves in collinear magnetic structures, Adv. Phys. **23**, 547 (1974).

[22] P. A. McClarty and J. G. Rau, Landau theory of altermagnetism, Phys. Rev. Lett. **132**, 176702 (2024).

[23] T. A. Maier and S. Okamoto, Weak-coupling theory of neutron scattering as a probe of altermagnetism, Phys. Rev. B **108**, L100402 (2023).

[24] M. Jamali, J. H. Kwon, S. M. Seo, K. J. Lee, and H. Yang, Spin wave nonreciprocity for logic device applications, Sci. Rep. **3**, 3160 (2013).

[25] S. Hayami, Y. Yanagi, and H. Kusunose, Bottom-up design of spin-split and reshaped electronic band structures in antiferromagnets without spin-orbit coupling: Procedure on the basis of augmented multipoles, Phys. Rev. B **102**, 144441 (2020).

[26] L. D. Yuan, Z. Wang, J. W. Luo, and A. Zunger, Prediction of low-Z collinear and noncollinear antiferromagnetic compounds having momentum-dependent spin splitting even without spin-orbit coupling, Phys. Rev. Mater. **5**, 014409 (2021).

[27] S. I. Pekar and E. I. Rashba, Combined resonance in crystals in inhomogeneous magnetic fields, Zh. Eksperim. Teor. Fiz. **47**, 1927 (1964).

[28] L. D. Yuan, Z. Wang, J. W. Luo, and A. Zunger, Strong influence of nonmagnetic ligands on the momentum-dependent spin splitting in antiferromagnets, Phys. Rev. B **103**, 224410 (2021).

[29] X. Zhou, W. Feng, R.-W. Zhang, L. Šmejkal, J. Sinova, Y. Mokrousov, and Y. Yao, Crystal thermal transport in altermagnetic RuO_2, Phys. Rev. Lett. **132**, 056701 (2024).

[30] O. Fedchenko, J. Minár, A. Akashdeep, S. W. D'Souza, D. Vasilyev, O. Tkach, L. Odenbreit, Q. Nguyen, D. Kutnyakhov, N. Wind *et al.*, Observation of time-reversal symmetry breaking in the band structure of altermagnetic RuO_2, Sci. Adv. **10**, eadj4883 (2024).

[31] T. Berlijn, P. C. Snijders, O. Delaire, H. D. Zhou, T. A. Maier, H. B. Cao, S. X. Chi, M. Matsuda, Y. Wang, M. R. Koehler, P. R.C. Kent, and H. H. Weitering, Itinerant Antiferromagnetism in RuO_2, Phys. Rev. Lett. **118**, 077201 (2017).

[32] L. D. Yuan, Z. Wang, J. W. Luo, E. I. Rashba, and A. Zunger, Giant momentum-dependent spin splitting in centrosymmetric low- Z antiferromagnets, Phys. Rev. B **102**, 014422 (2020).

[33] A. Bose, N. J. Schreiber, R. Jain, D.-F. Shao, H. P. Nair, J. Sun, X. S. Zhang, D. A. Muller, E. Y. Tsymbal, D. G. Schlom, and D. C. Ralph, Tilted spin current generated by the collinear antiferromagnet ruthenium dioxide, Nat. Electron. **5**, 267 (2022).

[34] H. Bai, L. Han, X. Y. Feng, Y. J. Zhou, R. X. Su, Q. Wang, L. Y. Liao, W. X. Zhu, X. Z. Chen, F. Pan, X. L. Fan, and C. Song, Observation of spin splitting torque in a collinear antiferromagnet RuO_2, Phys. Rev. Lett. **128**, 197202 (2022).

[35] S. Karube, T. Tanaka, D. Sugawara, N. Kadoguchi, M. Kohda, and J. Nitta, Observation of spin-splitter torque in collinear antiferromagnetic RuO_2, Phys. Rev. Lett. **129**, 137201 (2022).

[36] Z. H. Zhu, J. Strempfer, R. R. Rao, C. A. Occhialini, J. Pelliciari, Y. Choi, T. Kawaguchi, H. You, J. F. Mitchell, Y. Shao-Horn, and R. Comin, Anomalous antiferromagnetism in metallic RuO_2 determined by resonant x-ray scattering, Phys. Rev. Lett. **122**, 017202 (2019).

[37] S. W. Lovesey, D. D. Khalyavin, and G. van der Laan, Magnetic properties of RuO_2 and charge-magnetic interference in Bragg diffraction of circularly polarized x-rays, Phys. Rev. B **105**, 014403 (2022).

[38] S. W. Lovesey, D. D. Khalyavin, and G. van der Laan, Magnetic structure of RuO_2 in view of altermagnetism, Phys. Rev. B **108**, L121103 (2023).

[39] L. D. Landau and E. M. Lifshitz, On the theory of the dispersion of magnetic permeability in ferromagnetic bodies, Phys. Z. Sowjetunion **8**, 101 (1935).
[40] T. L. Gilbert, A phenomenological theory of damping in ferromagnetic materials, IEEE Trans. Magn. **40**, 3443 (2004).
[41] U. Nowak, Classical spin models, in *Handbook of Magnetism and Advanced Magnetic Materials*, edited by H. Kronmüller and S. Parkin (John Wiley & Sons, Hoboken, NJ, 2007).
[42] D. Hinzke and U. Nowak, Domain wall motion by the magnonic spin Seebeck effect, Phys. Rev. Lett. **107**, 027205 (2011).
[43] L. Kong and J. Zang, Dynamics of an insulating skyrmion under a temperature gradient, Phys. Rev. Lett. **111**, 067203 (2013).
[44] U. Ritzmann, D. Hinzke, and U. Nowak, Propagation of thermally induced magnonic spin currents, Phys. Rev. B **89**, 024409 (2014).
[45] A. Kehlberger, U. Ritzmann, D. Hinzke, E.-J. Guo, J. Cramer, G. Jakob, M. C. Onbasli, D. H. Kim, C. A. Ross, M. B. Jungfleisch, B. Hillebrands, U. Nowak, and M. Kläui, Length scale of the spin Seebeck effect, Phys. Rev. Lett. **115**, 096602 (2015).
[46] S. Selzer, U. Atxitia, U. Ritzmann, D. Hinzke, and U. Nowak, Inertia-free thermally driven domain-wall motion in antiferromagnets, Phys. Rev. Lett. **117**, 107201 (2016).
[47] A. Mook, R. R. Neumann, J. Henk, and I. Mertig, Spin Seebeck and spin Nernst effects of magnons in noncollinear antiferromagnetic insulators, Phys. Rev. B **100**, 100401(R) (2019).
[48] A. Donges, N. Grimm, F. Jakobs, S. Selzer, U. Ritzmann, U. Atxitia, and U. Nowak, Unveiling domain wall dynamics of ferrimagnets in thermal magnon currents: Competition of angular momentum transfer and entropic torque, Phys. Rev. Res. **2**, 013293 (2020).
[49] M. Weißenhofer and U. Nowak, Topology dependence of skyrmion Seebeck and skyrmion Nernst effect, Sci. Rep. **12**, 6801 (2022).
[50] K. Uchida, J. Xiao, H. Adachi, J. Ohe, S. Takahashi, J. Ieda, T. Ota, Y. Kajiwara, H. Umezawa, H. Kawai *et al.*, Spin Seebeck insulator, Nat. Mater. **9**, 894 (2010).
[51] U. Ritzmann, Modeling spincaloric Transport : Magnon accumulation and propagation, Ph.D. thesis, Universität Konstanz, Konstanz, 2015.
[52] R. Cheng, S. Okamoto, and D. Xiao, Spin Nernst effect of magnons in collinear antiferromagnets, Phys. Rev. Lett. **117**, 217202 (2016).
[53] S. Park, N. Nagaosa, and B.-J. Yang, Thermal Hall effect, spin Nernst effect, and spin density induced by a thermal gradient in collinear ferrimagnets from magnon–phonon interaction, Nano Lett. **20**, 2741 (2020).
[54] C. Stamm, C. Murer, M. Berritta, J. Feng, M. Gabureac, P. M. Oppeneer, and P. Gambardella, Magneto-optical detection of the spin Hall effect in Pt and W thin films, Phys. Rev. Lett. **119**, 087203 (2017).
[55] Y.-G. Choi, D. Jo, K.-H. Ko, D. Go, K.-H. Kim, H. G. Park, C. Kim, B.-C. Min, G.-M. Choi, and H.-W. Lee, Observation of the orbital Hall effect in a light metal Ti, Nature (London) **619**, 52 (2023).
[56] I. Lyalin, S. Alikhah, M. Berritta, P. M. Oppeneer, and R. K. Kawakami, Magneto-optical detection of the orbital Hall effect in chromium, Phys. Rev. Lett. **131**, 156702 (2023).
[57] T. Holstein and H. Primakoff, Field dependence of the intrinsic domain magnetization of a ferromagnet, Phys. Rev. **58**, 1098 (1940).
[58] N. N. Bogoljubov, V. V. Tolmachov, and D. V. Širkov, A new method in the theory of superconductivity, Fortschr. Phys. **6**, 605 (1958).
[59] J. G. Valatin, Comments on the theory of superconductivity, Nuovo. Cim. **7**, 843 (1958).
[60] J. Barker and Gerrit E. W. Bauer, Thermal spin dynamics of yttrium iron garnet, Phys. Rev. Lett. **117**, 217201 (2016).
[61] R. J. Elliott and M. F. Thorpe, The effects of magnon-magnon interaction on the two-magnon spectra of antiferromagnets, J. Phys. C: Solid State Phys. **2**, 1630 (1969).
[62] W. F. Brown, Thermal fluctuations of a single-domain particle, Phys. Rev. **130**, 1677 (1963).
[63] H. Ebert, D. Ködderitzsch, and J. Minár, Calculating condensed matter properties using the KKR-Green's function method–recent developments and applications, Rep. Prog. Phys. **74**, 096501 (2011).
[64] S. H. Vosko, L. Wilk, and M. Nusair, Accurate spin-dependent electron liquid correlation energies for local spin density calculations: A critical analysis, Can. J. Phys. **58**, 1200 (1980).
[65] S. L. Dudarev, G. A. Botton, S. Y. Savrasov, C. J. Humphreys, and A. P. Sutton, Electron-energy-loss spectra and the structural stability of nickel oxide: An LSDA+U study, Phys. Rev. B **57**, 1505 (1998).
[66] P. Strange, J. Staunton, and B. L. Gyorffy, Relativistic spin-polarised scattering theory-solution of the single-site problem, J. Phys. C **17**, 3355 (1984).